JOURNAL OF GEOPHYSICAL RESEARCH, VOL. 117, B08410, doi:10.1029/2012JB009241, 2012

Crustal deformation along the Dead Sea Transform and the Carmel Fault inferred from 12 years of GPS measurements

M. Sadeh,[1,2,3] Y. Hamiel,[2] A. Ziv,[1,3] Y. Bock,[4] P. Fang,[4] and S. Wdowinski[5]

Received 20 February 2012; revised 27 June 2012; accepted 30 June 2012; published 17 August 2012.

[1] Large-scale crustal deformation in the Levant is mainly related to the DST and the CFS. The former is an active left lateral transform, bounding the Arabian plate and the Sinai sub-plate, and the latter branches out of the former and separates the Sinai sub-plate into two tectonic domains. In this study we obtain the velocities of 33 permanent GPS stations and 145 survey stations that were surveyed in three campaigns between 1996 and 2008. We use a simple 1-D elastic dislocation model to infer the slip rate and locking depth along various segments of the DST. We infer a 3.1–4.5 mm/yr slip rate and a 7.8–16.5 km locking depth along the DST north of the CFS, and a slip rate of 4.6–5.9 mm/yr and locking depth of 11.8–24 km along the Jericho Valley, south of the CFS. Further south, along the Arava Valley we obtain a slip rate of 4.7–5.4 mm/yr and a locking depth of 12.1–23 km. We identify an oblique motion along the Carmel Fault with ~0.7 mm/yr left-lateral and ~0.6 mm/yr extension rates, resulting in N-S extension across the Carmel Fault. This result, together with the decrease in DST slip velocity from the Jericho Valley to the segment north of the CFS, confirms previous suggestions, according to which part of the slip between Arabia and Sinai is being transferred from the DST to the CFS.

Citation: Sadeh, M., Y. Hamiel, A. Ziv, Y. Bock, P. Fang, and S. Wdowinski (2012), Crustal deformation along the Dead Sea Transform and the Carmel Fault inferred from 12 years of GPS measurements, *J. Geophys. Res.*, *117*, B08410, doi:10.1029/2012JB009241.

1. Introduction

[2] Tectonic deformation in the Levant is primarily related to the Dead Sea Transform (DST), a ~1000 km long continental transform fault forming the tectonic boundary between the Arabian plate and the Sinai sub-plate (Figure 1). The DST dates back to the mid-Cenozoic era, 18–20 ma ago [*Eyal et al.*, 1981; *Garfunkel*, 1981; *Joffe and Garfunkel*, 1987]. The principal movement along the DST is left-lateral, which according to several geological markers across the southern part of the DST, resulted in a maximum total horizontal offset of about 105 km [*Quennell*, 1959; *Freund et al.*, 1968, 1970]. A major fault system within the Sinai sub-plate is the Carmel-Gilboa-Faria Fault System (CFS) that consists of NW-SE trending faults, extending from the central part of the Jordan Valley to the Mediterranean Sea near the northwestern tip of Mt. Carmel (Figure 2). Along the northern section of the Carmel Fault (Figure 2) left-lateral transtensional motion had been inferred, with total left-lateral and vertical displacements of 3–10 km [*de Sitter*, 1962; *Freund et al.*, 1970] and 0.3–1.5 km [*Picard and Kashai*, 1958; *Achmon*, 1986], respectively. Since the total displacement is rather small, it is difficult to assess the long term slip rate along the Carmel Fault.

[3] Precise GPS measurements reveal the relative interseismic surface velocities and shed light on the present fault kinematics along the DST. Slip rates in the range of 4.3–6.0 mm/yr were obtained by computing the relative motion along the Arabia-Sinai plate boundary with respect to a geodetically defined Euler pole [*McClusky et al.*, 2003; *Wdowinski et al.*, 2004; *Reilinger et al.*, 2006; *Vigny et al.*, 2006; *Le Beon et al.*, 2008]. Based on velocities at 13 permanent GPS sites in Israel and Syria, *Wdowinski et al.* [2004] inferred a slip rate of 3.7 ± 0.4 mm/yr (employing a fixed locking depth of 12 km) along the central part of the DST extending from the Hula Basin to the Arava Valley (Figure 2). *Al-Tarazi et al.* [2011] inferred a slip rate of 4.7 ± 0.4 mm/yr and locking depth of 8 ± 5 km along the Jordan Valley based on data from 18 stations in Israel and Jordan. Along the Arava Valley, *Al-Tarazi et al.* [2011] inferred a slip rate of 4.9 ± 0.4 mm/yr and a locking depth of 15 ± 5 km using 36 stations, in agreement with the 4.9 ± 1.4 mm/yr slip rate

[1]Department of Geological and Environmental Sciences, Ben-Gurion University of the Negev, Beer-Sheva, Israel.
[2]Geological Survey of Israel, Jerusalem, Israel.
[3]Department of Geophysical, Atmospheric and Planetary Sciences, Tel Aviv University, Tel-Aviv, Israel.
[4]Institute of Geophysics and Planetary Physics, Scripps Institution of Oceanography, La Jolla, California, USA.
[5]Rosenstiel School of Marine and Atmospheric Science, University of Miami, Miami, Florida, USA.

Corresponding author: M. Sadeh, Department of Geophysical, Atmospheric and Planetary Sciences, Tel Aviv University, Tel-Aviv 69978, Israel. (maytalsadeh@tau.ac.il)

0148-0227/12/2012JB009241

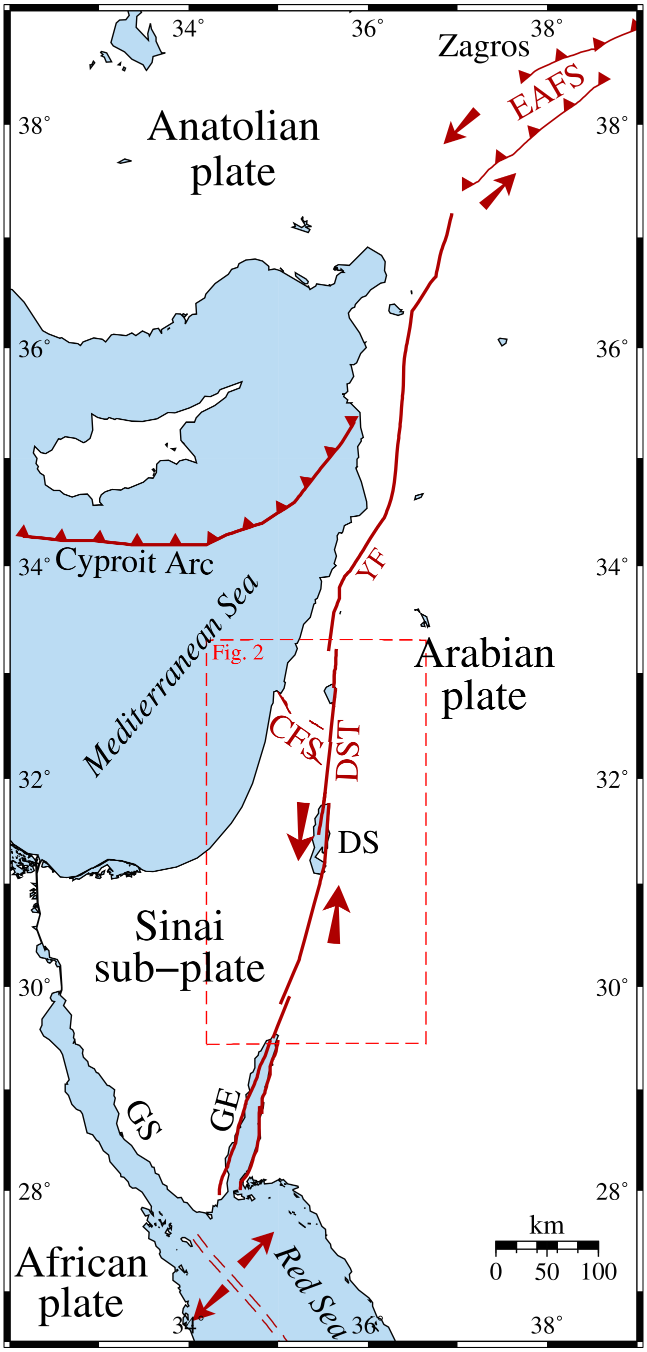

Figure 1. Tectonic map of the eastern Mediterranean, showing the plate boundaries and the main faults. Abbreviations: DST, Dead Sea Transform; CFS, Carmel Fault System; YF, Yammouneh Fault; GE, Gulf of Eilat; GS, Gulf of Suez. The dashed rectangle indicates the boundaries of the map in Figure 2.

and 11.5 ± 10.2 km locking depth obtained by *Le Beon et al.* [2008] based on 18 GPS stations located on either side of the fault. Previous attempts to determine the current slip rates along the Carmel Fault using geodetic measurements yielded ambiguous results [*Agmon*, 2001; *Ostrovsky*, 2005; *Nof*, 2006; *Reinking et al.*, 2011].

[4] In this study we use GPS raw observations measured at 145 survey and 18 permanent stations in Israel between 1996 and 2008. This geodetic data set is the most numerous, most densely spaced, spanning the longest interval and occupying the largest area used so far in Israel. Using this unique data set, we calculate the Euler pole and rotation rate of the Sinai sub-plate with respect to the ITRF2005 reference frame, obtain a map of surface velocities in Israel relative to Sinai and infer the slip rates and locking depths along different segments of the DST and the Carmel Fault. Finally, we compare the geodetically determined locking depth and the seismicity cutoff depth, and discuss the implications for seismic hazard assessment based on our results and previously reported archeo-seismic, paleo-seismic and historical records.

2. Data Acquisition and Processing

2.1. G1 Local Survey Network

[5] The G1 geodetic-geodynamic survey network was established in 1996 by the Geological Survey of Israel (GSI) and the Survey of Israel (SOI) [*Melzer*, 1996]. It consists of 145 rock-anchored benchmarks placed throughout Israel with a spacing of 10–20 km (Figure 2). The network has been surveyed in 1996–1997, 2001–2002 and 2008 using the equipment listed in Table 1. Four nearby stations were measured simultaneously during each day of measurements, and in order to strengthen the network, one or two of those stations were included in the set of four stations measured the following day. In this way, stations were measured 2–5 times in each survey for ~24 hours during the first survey and 8–12 hours during subsequent surveys. The large number of visits (4–12) to each station helps to detect outliers and average out transient effects on each measurement, and it therefore compensates for the relatively short measurement durations.

2.2. Regional Permanent Network

[6] In order to complement the local network and link it to a global reference frame, 33 regional continuous GPS (CGPS) stations were used, consisting of all 18 CGPS stations in Israel (referred to as the GIL network, green squares in Figure 2) [*Wdowinski et al.*, 2001] and 15 additional stations in the Eastern Mediterranean and the Middle East (Figure 3).

[7] Considerations of site stability, location and operation interval were taken into account while choosing the stations. The observation epochs used in the final solution are shown in Figure 4. Raw observations were downloaded from Scripps Orbit and Permanent Array Center (SOPAC, http://sopac.ucsd.edu/dataArchive) and UNAVCO (http://facility.unavco.org/data) websites.

2.3. Processing Method

[8] GPS phase observations were analyzed using the GAMIT/GLOBK software package version 10.35 [*Herring et al.*, 2009]. First, GPS phase observations of the regional network were used in GAMIT to compute precise baseline components, loosely constrained position estimates, zenith delays at each site, and orbital and Earth orientation parameters. Between July 1996 and December 2008, these daily solutions were obtained using a day per week data interval. Additionally, for days at which local survey sites were measured, data from both regional and local sites were analyzed

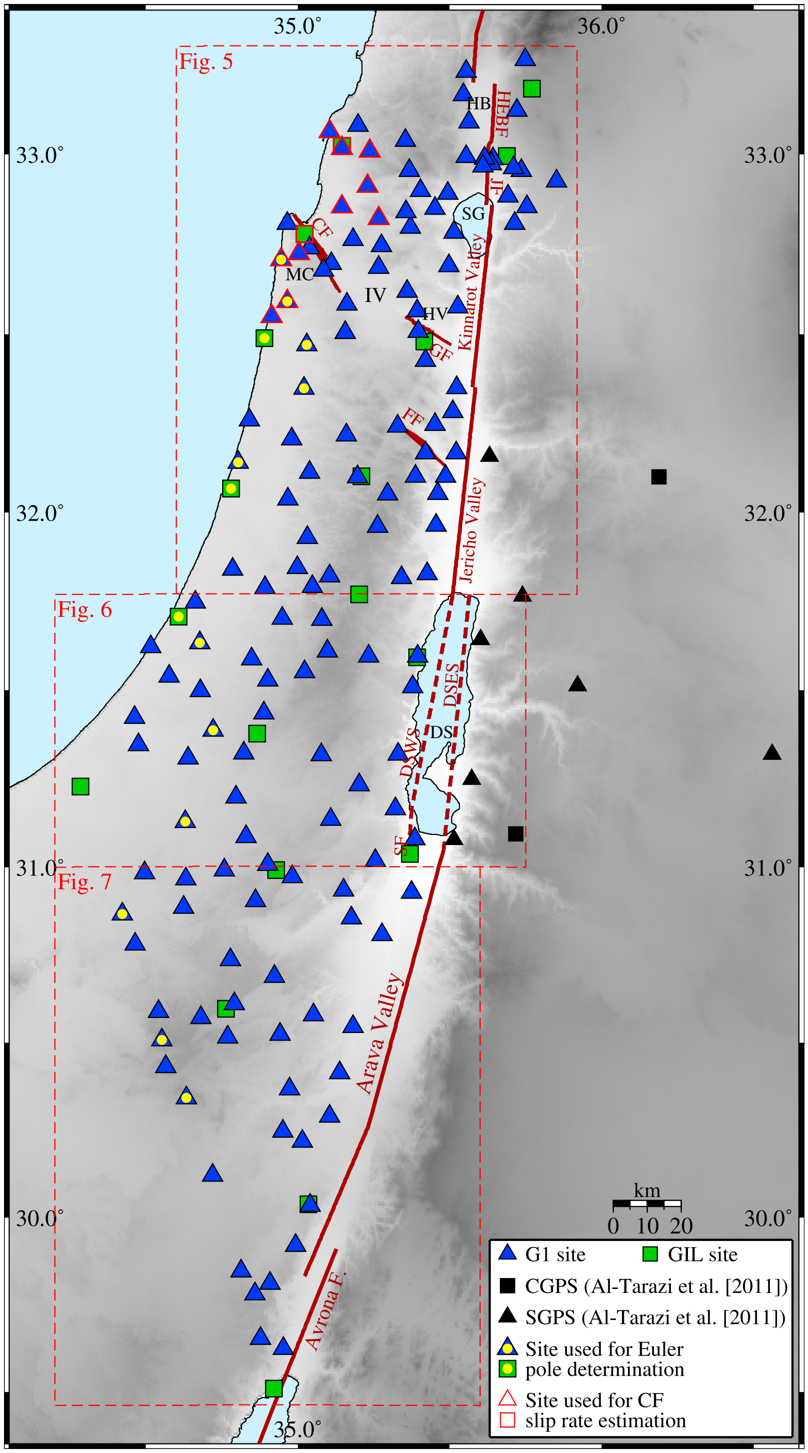

Figure 2. Map of the study area, showing the G1 survey (blue triangles) and GIL permanent (green squares) sites, CGPS and Survey GPS (SGPS) sites reported by *Al-Tarazi et al.* [2011] (black squares and triangles, respectively). Symbols filled with yellow dots indicate sites that are used for the determination of the Sinai-ITRF2005 Euler pole, and symbols outlined in red indicate sites that are used to infer the Carmel fault slip rate. Dark red lines indicate location of the main faults in the study area. Abbreviations: HB, Hula Basin; HEBF, Hula east boundary fault; JF, Jordan Fault; MC, Mt. Carmel; IV, Izra'el Valley; HV, Harod Valley; CF, Carmel Fault; GF, Gilboa Fault; FF, Faria Fault; DSES, Dead Sea eastern strand; DSWS, Dead Sea western strand; DS, Dead Sea; SF, Sedom Fault.

Table 1. Equipment Used in G1 Surveys

Survey	Receiver	Antenna
1996–1997	TRIMBLE 4000SSE	TRIMBLE TRM22020.00+GP
2001–2002	TRIMBLE 5700	TRIMBLE TRM41249.00
2008	LEICA GX1230GG	LEICA LEIAT504GG

jointly. Daily GAMIT solutions were subsequently used as quasi-observations in GLOBK to obtain position time series for all sites. These were carefully inspected to detect and remove outliers and unstable data segments, and detect and account for offsets caused by equipment change. Next, site coordinates and velocities were estimated, by minimizing the departure from a priori values of coordinates and velocities of most permanent sites with respect to an ITRF2005 no-net-rotation reference frame available at SOPAC's site.

[9] Coordinates and velocities of campaign sites computed in GLOBK were used as a priori data for an additional GAMIT calculation of the local network, this time with tighter constraints of 2–3 cm applied to the location of all survey sites. The improved solutions were used as before to estimate a final set of site coordinates and velocities with respect to ITRF2005. The weighted RMS of the residual velocities for the sites used to define the reference frame are 0.95, 1.21 and 1.57 mm/yr for the east, north and vertical components, respectively. In order to account for the underestimation of the true uncertainties by the processing software [*Zhang et al.*, 1997; *Mao et al.*, 1999], horizontal and vertical random walk noise of 0.38 and 0.8 mm/$\sqrt{\text{yr}}$, respectively were added to all permanent sites, and horizontal and vertical random walk noise of 0.75 and 4 mm/$\sqrt{\text{yr}}$, respectively were added to all survey sites.

3. Results

3.1. Sinai and Arabia Euler Poles

[10] The Euler pole of the Sinai rigid plate with respect to ITRF2005 is computed using the horizontal velocities of 14 sites (denoted by yellow dots in Figure 2) that are chosen for their large distance from the DST, where the deformation associated with the slip along the DST is minimal. This Euler pole (N56.642, E330.836 and Ω = 0.35 deg/Myr), as well as those reported in previous studies are listed in Table 2. Since the Sinai sub-plate is relatively small and narrow, and its Euler pole of rotation with respect to ITRF is located at a distance that is much larger than the plate's dimensions, the locations of the Sinai-ITRF Euler poles are rather loosely constrained. Nevertheless, note that despite the different GPS sites and observation intervals used in calculating these poles, the poles listed in Table 2 are fairly close. Note also that the Euler pole longitudes are not as well constrained as their latitudes, and that a trade-off exists between the longitude and the rotation magnitude (Table 2).

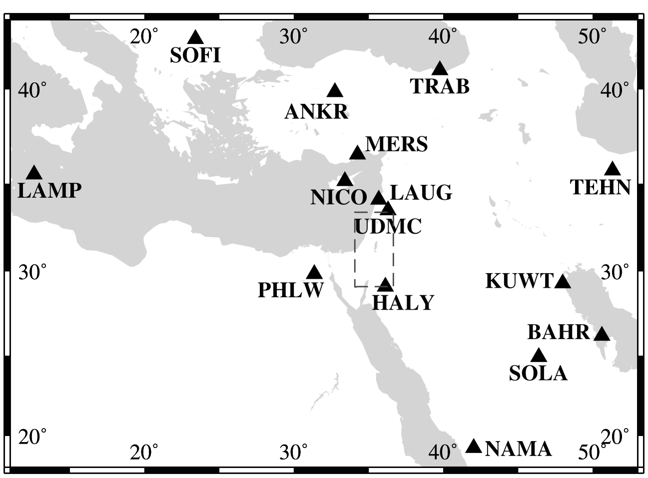

Figure 3. Regional CGPS sites used in this study in addition to the GIL network. Dashed box indicates the study area in Figure 2.

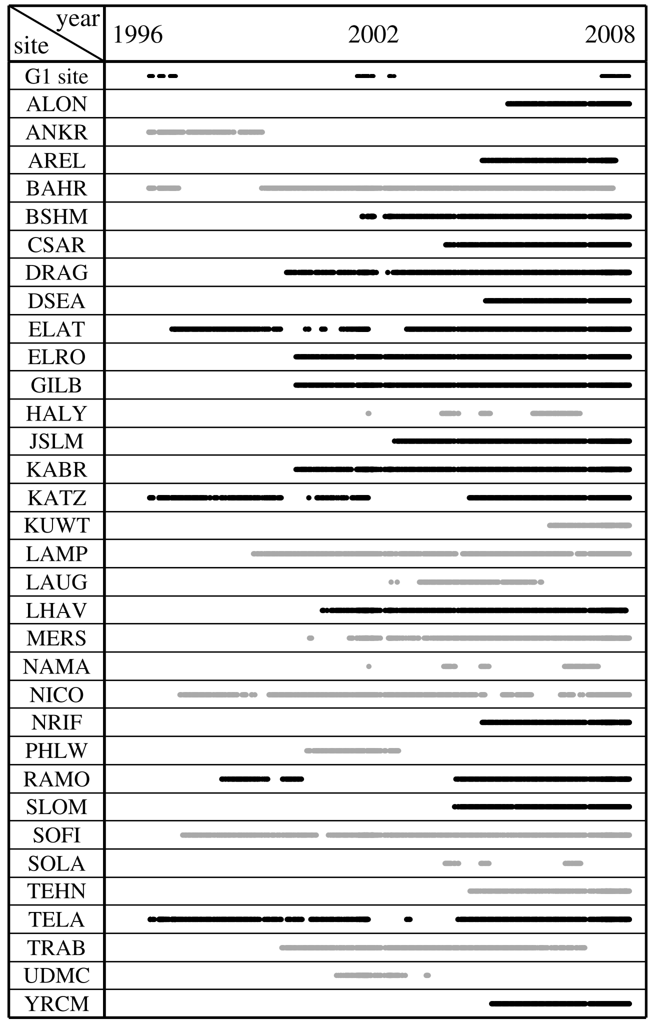

Figure 4. Observation epochs of all GPS sites used in this study. Time lines show the epochs during which each site has operated successfully. Thin and thick dark lines denote G1 and GIL sites, respectively, and the grey lines denote CGPS regional sites.

3.2. Velocity Field

[11] Site velocities are obtained in ITRF2005 and Sinai Reference Frames (SRF), and are listed along with their 1σ uncertainties in Table S1 of the auxiliary material.[1] Because the deformation rates associated with the DST and the CFS

[1]Auxiliary materials are available in the HTML. doi:10.1029/2012JB009241.

Table 2. Sinai-ITRF Euler Poles Obtained in This Study and in Previous Studies

Location		Error Ellipse			Rotation Rate (deg/Myr)		
Latitude (°N)	Longitude (°E)	ΔLat.	ΔLon.	Azimuth[a]	Ω	ΔΩ	Reference
				Sinai-ITRF2000			
57.980	334.890	0.31	26.59	96.4	0.3592	0.104	*Wdowinski et al.* [2004]
53.520	359.090	0.56	16.85	64.0	0.477	0.150	*Le Beon et al.* [2008]
54.228	352.193	0.17	9.31	161.0	0.438	0.066	SOPAC
				Sinai-ITRF2005			
56.642	330.836	0.206	10.257	134.74	0.35	0.029	This study

[a]Clockwise angle between north and the semi-major ellipse axis.

are small compared with other plate boundaries, the signal-to-noise ratio within the study area is relatively small. Nevertheless, the velocity field is very clearly reflecting the tectonic deformation, and the most prominent pattern apparent in the velocity field is the increase in the DST-parallel velocities from the Mediterranean coast toward the DST fault zone and more so east of it, reflecting the left-lateral motion below the locking depth between Sinai and Arabia (Figure 5). Note, however, that such a velocity gradient is not observed from the Mediterranean to the Dead Sea Basin (Figure 6). Another clear deformation pattern is the relatively high northward velocity of most sites located north of the CFS with respect to sites located south of it (Figure 5).

[12] Careful inspection of the velocity field reveals some smaller scale deformation patterns. Sites KNNW, KNSW, KNNE and KNSE located close to the Jordan Fault in northern Israel (Figure 5) exhibit a relatively fast eastward motion, which may reflect local deformation in this area. Further to the south, sites SDLA, MALS, ARMN, MSUA, BKOT, GTIT and MCRA, located near the intersection between the DST and the CFS (Figures 2 and 5), seem to rotate counterclockwise. In addition, the northwards velocities of sites SDLA, MALS, ARMN and MSUA are more than 1 mm/yr faster than those of sites BKOT, GTIT and MCRA that are located just a few kilometers to the west. Together, the rotational movement and the steep velocity gradient suggest that the deformation in this region is affected by the interaction between the DST and the CFS. Near the Mediterranean coast, the permanent GIL site SLOM that is located atop a building shows a clear anomalous behavior. It is evident from its time series, velocity (Figure 6) and site observations that its motion reflects site instability, rather than a true ground motion.

3.3. Slip Rate and Locking Depth Inversions

[13] The slip rate and locking depth are inferred using the screw dislocation model of *Savage and Burford* [1973], according to which the fault plane is vertical, infinitely long, embedded within a homogeneous elastic half-space and slips horizontally. Consequently, the ground velocities are strike-parallel and are a function of the distance from the fault plane. Ground velocity, V, as a function of distance, x, from the fault plane is:

$$V(x) = V_1 + \frac{V_0}{\pi}\tan^{-1}\left(\frac{x}{D}\right), \quad (1)$$

where V_1 is the velocity of the fault plane relative to a fixed reference frame and D (≥ 0) is the depth below which the slip rate is constant and is equal to V_0. Hereafter, V_0 and D are referred to as the slip rate and locking depth, respectively. The long-term slip rates, the locking depths (and also V_1) and their uncertainties along different segments of the DST and the CFS are solved for using a least-squares criterion coupled with a Monte Carlo procedure that accounts for uncertainties in fault position and station velocities. The location of each fault segment is set based on the map of active faults in Israel [*Bartov et al.*, 2000] and other studies [*Garfunkel et al.*, 1981; *Reches and Hoexter*, 1981; *Rotstein and Bartov*, 1989; *van Eck and Hofstetter*, 1990; *Marco et al.*, 1997; *Klinger et al.*, 2000; *Hurwitz et al.*, 2002; *Marco et al.*, 2005; *Bartov et al.*, 2006; *Hofstetter et al.*, 2007; *Makovsky et al.*, 2008]. In each Monte Carlo simulation, the fault planes are perturbed randomly by ± 0.5 km and fault-parallel velocities are perturbed by the 2σ uncertainty of the data using uncorrelated Gaussian random distribution. Results presented below are based on the statistics of 10^5 such Monte Carlo simulations, and are at 68% confidence level.

[14] In principle it is advantageous to invert model parameters using as much data as possible, and for that reason it is sensible to complement our data set with previously published data. However, the merging of different data sets from different studies has two disadvantages. The first is that the result may be affected by the differences in data collection and processing approach used by the different research groups, and the second is that transforming the velocity field from one reference frame to another may introduce an error. Thus in this study we only merge data from previous studies in cases where use of our data alone does not constrain the slip rate and/or the locking depth.

[15] Anomalous behavior of certain sites with respect to surrounding sites for no obvious tectonic reason, is due to either local deformation or bad measurements. Because the inclusion of the velocities measured at these sites (white arrows in Figures 5–7) in the analyses is undesirable, they are excluded from the inversions of slip rates and locking depths.

3.3.1. The DST North of the CFS

[16] GPS sites included in the inversion of the slip rate and the locking depth along the Hula east boundary fault, Jordan Fault and Kinnarot Valley segments are enclosed within rectangle (a) in Figure 5. We exclude from the inversion the sites located at a distance of less than 15 km from the CFS, and the ADMT site, whose velocity is anomalous with respect to nearby sites (e.g., NHRI, CBRI, ECOV and MTAT). The slip rate and the locking depth estimates are 3.1–4.5 mm/yr and 7.8–16.5 km, respectively, with the most probable solution corresponding to 3.8 mm/yr and 12.4 km

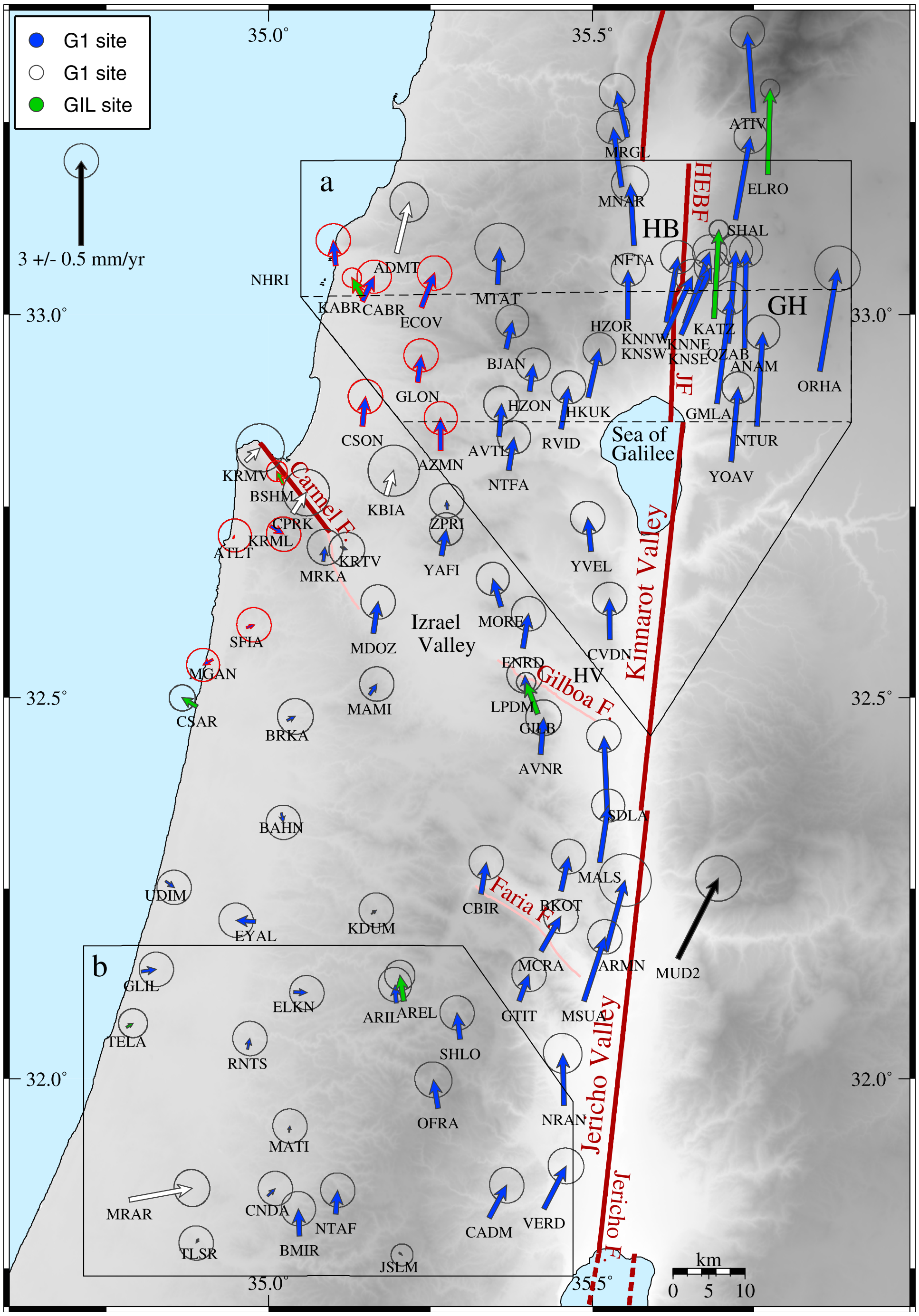

Figure 5. Horizontal velocity map of North Israel and the Jericho Valley. Dark red lines denote the fault traces used for the computation of the slip rates and locking depths, and pink lines are additional faults that are part of the CFS. Green arrows denote GIL sites, blue arrows denote G1 sites, white arrows denote the G1 sites excluded from the inversion of the slip rates and locking depths and the black arrow denotes a site from *Al-Tarazi et al.* [2011]. Arrows outlined in red denote sites that are used for the inversion of slip rate along the Carmel's northern segment. The northern (labeled as "a") and southern solid (labeled as "b") rectangles enclose sites that are used for the calculation of the slip rates and locking depths along the Northern Israel segment and the Jericho Valley, respectively. Sites enclosed within the two dashed lines in rectangle "a" are used for the inversion of the Jordan Fault slip rate and locking depth. Abbreviations: HB, Hula Basin; GH, Golan Heights; JF, Jordan Fault; HV, Harod Valley.

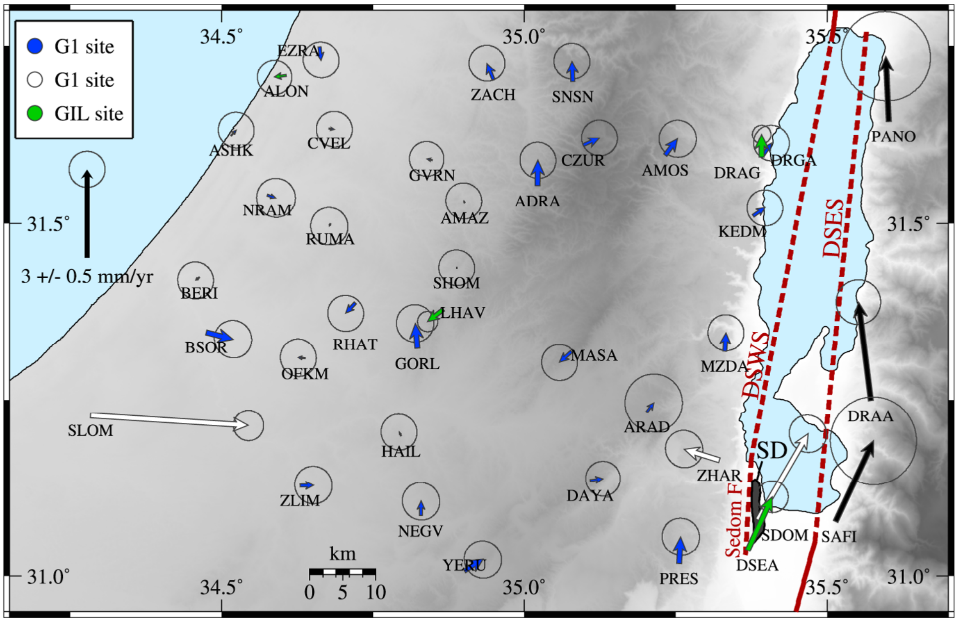

Figure 6. Horizontal velocity map of the Dead Sea region. Dark red dashed lines denote the fault traces used for the computation of the slip rates and locking depths. Green arrows denote GIL sites, blue arrows denote G1 sites, white arrows denote the sites that are excluded from the inversion of the slip rates and locking depths and black arrows denote sites from *Al-Tarazi et al.* [2011]. Abbreviations: DSES, Dead Sea eastern strand; DSWS, Dead Sea western strand; SD, Sedom Diapir.

(Figure 8a). Sites included in the inversion of the slip rate and the locking depth along the Jordan Fault alone, for which dense data on either side of the fault are available, are located between the two dashed lines in Figure 5. A slip rate of 3.2–4.4 mm/yr and a locking depth of 5.9–13.4 km are inferred for this fault, with the most probable solution corresponding to a slip rate of 3.7 mm/yr and a locking depth of 8.7 km (Figure 8b). For the geodetic measurements to capture most of the slip across the fault, measurements should be made across a zone that is several times wider than the locking depth [*Savage and Burford*, 1973]. Owing to the lack of data far from the fault zone, the positive correlation between the modeled locking depth and the slip rate along these fault segments is strong (Figures 8a and 8b).

3.3.2. The Jericho Valley

[17] While the overall fault-parallel velocity gradient of sites enclosed within rectangle (b) in Figure 5 increases toward the Jericho Valley in a manner that is consistent with the simplified dislocation model of equation (1), slip rates and locking depths cannot be constrained using our data due to the lack of sites near the fault. Therefore, we complement our data set with velocities reported by *Al-Tarazi et al.* [2011]. Prior to incorporating these velocities into our analysis, we estimate the translation and rotation that minimizes the residual misfit between the horizontal velocities of 16 permanent stations common to *Al-Tarazi et al.* [2011] and this study. The RMS misfit between our velocities and the transformed velocities of *Al-Tarazi et al.* [2011] is 0.49 mm/yr. Using our velocities and the transformed velocities of sites HUGS and MUD2 located in Jordan, east of the Jericho Valley and within it's northern and southern ends at latitudes 32.175 and 31.75, respectively, we infer a slip rate of 4.6–5.9 mm/yr and locking depth of 11.8–24 km with the most probable solution corresponding to 4.9 mm/yr and 15.8 km, respectively (Figure 9a).

3.3.3. The Dead Sea Basin

[18] Faulting geometry within the Dead Sea Basin is rather complex, including faults striking at different orientations and slipping at different directions [*Garfunkel and Ben-Avraham*, 1996; *Lazar et al.*, 2006; *Shamir*, 2006]. Nevertheless, most of the left-lateral slip in that region is likely to be accommodated along the western and/or eastern strands of the DST [e.g., *Garfunkel*, 1981; *Lazar et al.*, 2006] (Figure 6). The absence of northward displacement increase from the Mediterranean coast to the western strand of the DST within the basin (Figures 6 and 9b) is consistent with three different scenarios: (1) Slip along the Sedom Fault, and possibly also along the western strand further north is mostly aseismic. (2) relatively small slip occurs along the western strand of the DST while the motion between Sinai and Arabia is accommodated mainly along the eastern strand. In that case, the increase in fault parallel velocities is expected to occur within the basin, where only one reliable site is available (the permanent site DSEA in Figure 6). (3) The total slip is distributed among several faults. Since the available data cannot constrain complex models with several faults slipping simultaneously, we examine scenarios (1) and (2).

[19] Slip rate and locking depth inversions using our data alone failed to converge. For this reason we complement our data with velocities of sites that are located east of the Dead Sea [*Al-Tarazi et al.*, 2011] (see black symbols in Figure 2). The velocities of those sites are transformed to the SRF by minimizing the misfit RMS of sites that are common to *Al-Tarazi et al.* [2011] and this study. Two sites are excluded from the inversion (see white arrows in Figure 6), the ZHAR site whose velocity is anomalous and the SDOM site, which

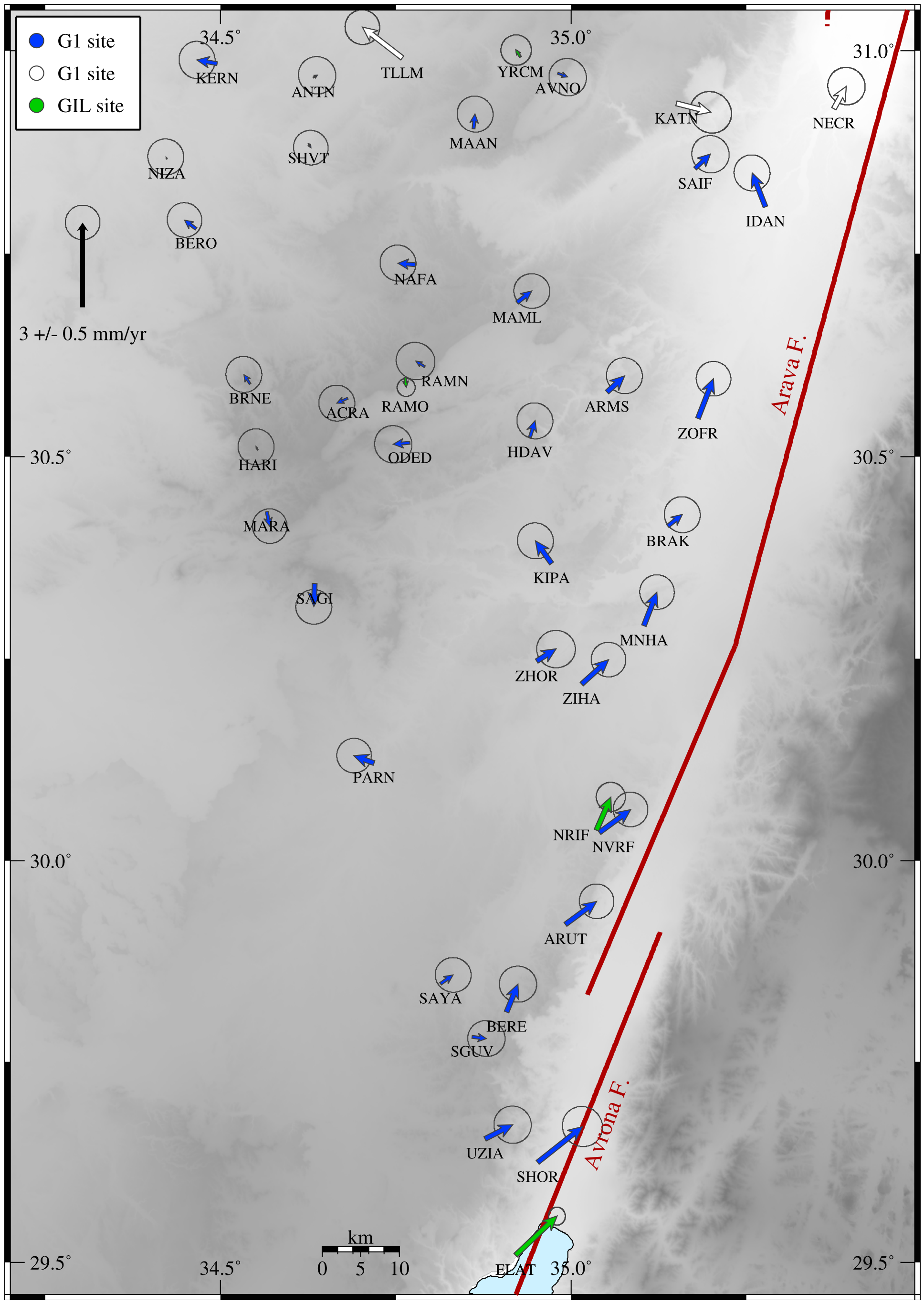

Figure 7. Horizontal velocity map of the Arava Valley region. Dark red lines denote the fault traces used for the computation of the slip rates and locking depths. Green arrows denote GIL sites, blue arrows denote G1 sites and white arrows denote the G1 sites excluded from the inversion of the slip rates and locking depths.

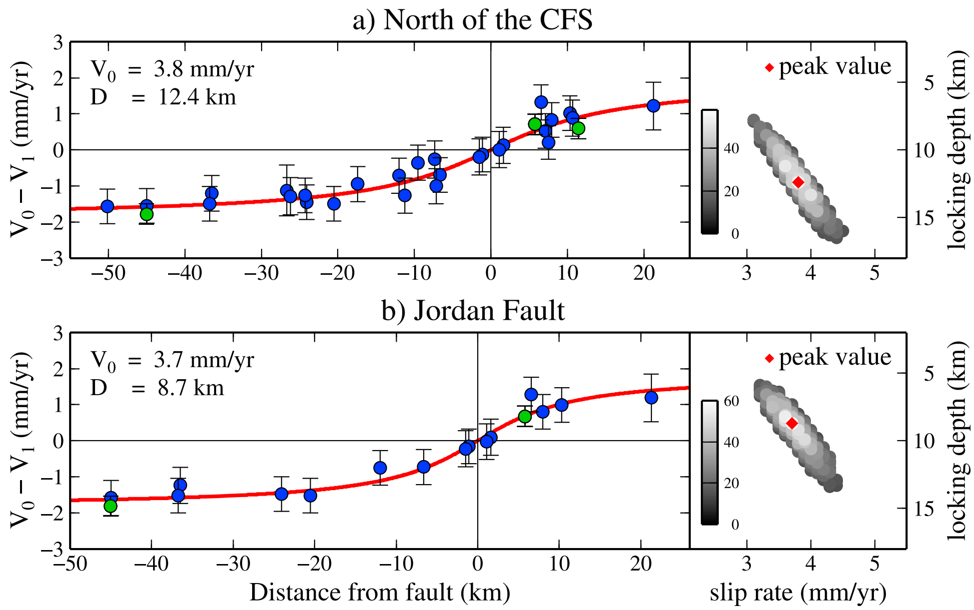

Figure 8. Fault parallel velocities and fit to 1-D dislocation model for the following DST segments: (a) north of the CFS (stations are enclosed by solid rectangle (a) in Figure 5) and (b) the Jordan Fault (subset of the stations used in Figure 8a, which are enclosed by the dashed black lines in Figure 5). Red curves on left-hand panels show the most probable fit to equation (1), and blue and green symbols denote G1 and GIL stations, respectively. Right-hand panels show the result of slip rate and locking depth inversions within a 1σ confidence level, using a Monte Carlo approach to account for the data uncertainties. The color code corresponds to the frequency of each solution calculated on a grid of 0.1 km by 0.1 mm/yr, and the red diamond denotes the most frequent solution.

is located atop of the rising Sedom diapir and whose velocity is strongly affected by the local deformation at that location.

[20] We obtain a slip rate of 3.5–3.9 mm/yr and a locking depth of 3.6–6.3 along the western strand of the DST (Figure 9b). Although the results seem to be well constrained on a velocity versus locking depth diagram, they are not realistic for this area. Not only that the slip rate is significantly slower than those obtained along the Jericho Valley and the Arava Valley (see below), but earthquakes in this area are reported at much greater depths than the modeled locking depth [*Aldersons et al.*, 2003]. For a scenario where most of the relative motion between the plates is accommodated along the eastern strand, we infer a slip rate of 4.5–5.1 mm/yr and a locking depth of 12–17.6 km (Figure 9c). This slip rate is closer to that expected based on the information gained in previous studies [e.g., *Reilinger et al.*, 2006; *Le Beon et al.*, 2008] and the results obtained in this study for the Jericho and the Arava segments (see sections 3.3.2 and 3.3.4). Yet, the large scatter of the velocities east of the DST and the large misfit between the velocity of site DSEA and the preferred model imply that this result may not reflect the true slip distribution along the Dead Sea Basin.

3.3.4. The Arava Valley

[21] Based on the velocities of GPS sites that are located south of latitude 31N and west of the fault (Figure 7) and site HALY that is located east of the fault and within the Arabian plate (Figure 3) we infer a slip rate of 4.7–5.4 mm/yr and a locking depth of 12.1–23 km (Figure 9d) along the Arava Valley. The result with the highest probability to fit the data is 5.1 mm/yr and 15.5 km for the slip rate and locking depth, respectively (Figure 9d). Note that here, owing to the inclusion of GPS sites that are located as far as 90 km into the Sinai sub-plate, there is no trade-off between the slip rate and locking depth, and the slip rate is better constrained than the locking depth.

[22] In Figure 9e we show the result of an additional inversion, this time without HALY, the permanent station 120 km inside the Arabian plate. Note that despite this inversion being based solely on sites located west of the DST, it yields a slip rate and locking depth similar to those obtained in studies accounting for velocities on either side of the fault [*Le Beon et al.*, 2008; *Al-Tarazi et al.*, 2011]. This result is a consequence of the model being symmetric and continuous (arctan) and the data being of high quality and well distributed with respect to the fault plane.

3.3.5. The CFS

[23] In order to estimate the rate of relative horizontal slip across the CFS, the fault parallel and fault perpendicular velocities relative to the westernmost segment of the Carmel fault (dark red line in Figure 5) are examined. Special attention is given to this segment of the CFS because the deformation zone in this area is the narrowest and because it is located sufficiently far from the DST, where the contribution of the ground displacement due to slip along the DST is less than 0.1 mm/yr. For this analysis, we use 12 sites located on either side of the fault and at a distance greater than 30 km from the DST (these sites are outlined in red in Figure 5). Note the notably larger uncertainties of CPRK, KRMV and KBIA with respect to other nearby sites. These larger uncertainties are attributed mainly to their shorter temporal

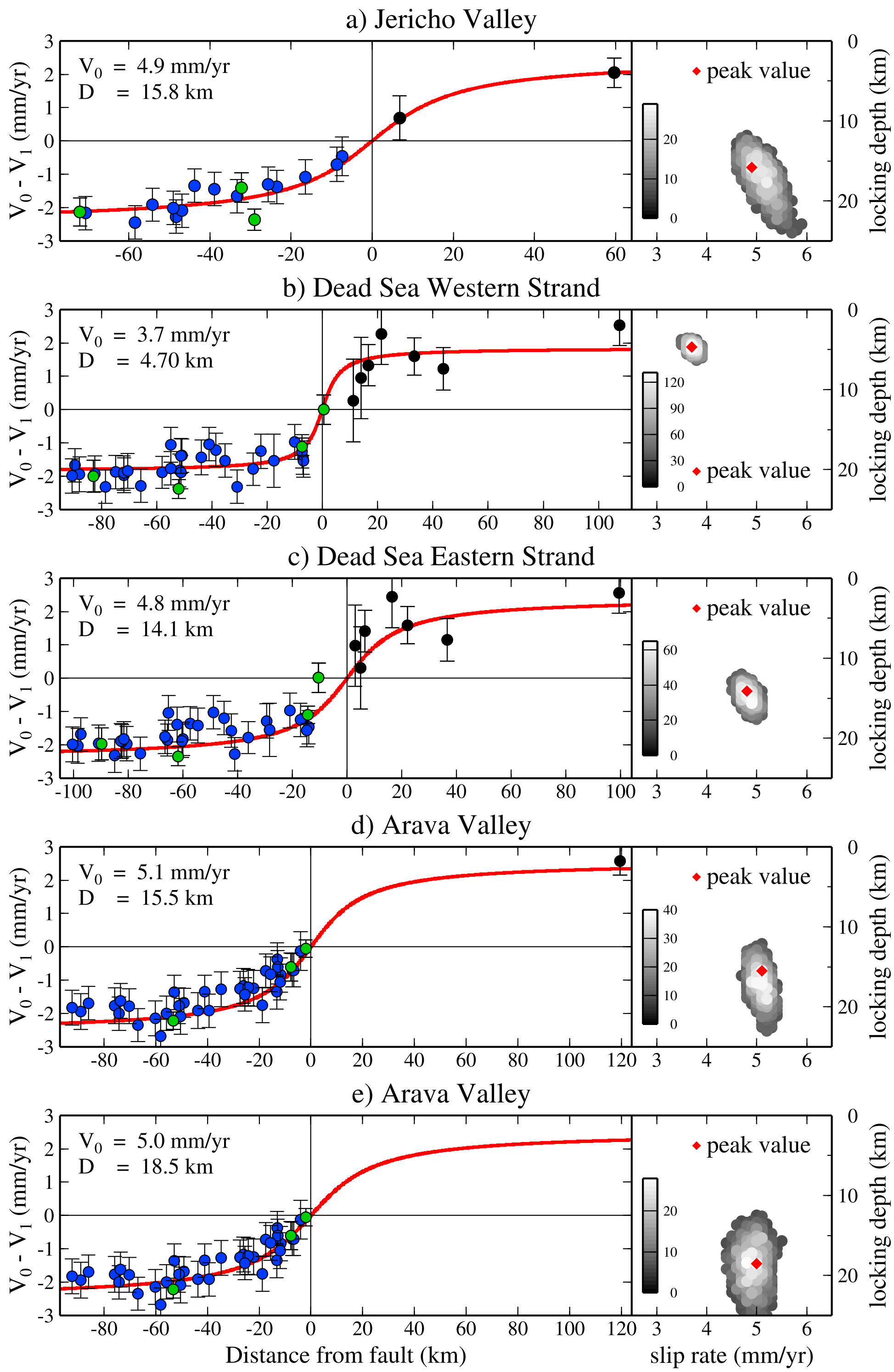

Figure 9. Fault parallel velocities and fit to inter-seismic model for the following DST segments: (a) Jericho Valley, (b) the Dead Sea western strand, (c) the Dead Sea eastern strand, (d) Arava Valley including HALY and (e) Arava Valley excluding HALY. Red curves on left-hand panels show the most probable fit to equation (1). Blue and green symbols denote G1 and GIL stations, respectively and black symbols denote sites located on the Arabian plate. Right-hand panels show the result of slip rate and locking depth inversions, using a Monte Carlo approach to account for the data uncertainties. The color code corresponds to the frequency of each solution calculated on a grid of 0.1 km by 0.1 mm/yr.

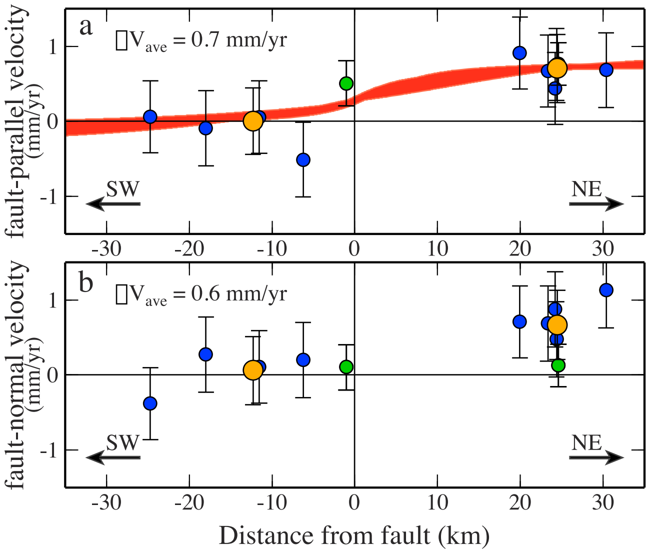

Figure 10. Profiles of velocity versus distance for the Carmel Fault. (a) Carmel fault-parallel velocity. Positive values indicate NW horizontal motion. The red area indicates the range of model solutions for locking-depths between 5–20 km and northeast dipping angle between 60°–90°. (b) Carmel fault-normal velocity. Positive values indicate NE horizontal motion. Blue and green symbols denote survey and permanent GPS stations, respectively. Orange symbols denote the average velocity of stations on either side of the Carmel Fault.

baseline (they were only surveyed in 2002 and 2008). Since the signal we are seeking to resolve is especially small, these stations are disregarded. Another nearby site that is disregarded is MRKA, which is situated within an active N-S trending fault zone (Figure 5).

[24] Use of a simple dislocation model to infer the left-lateral slip rate and locking-depth is problematic due to the slip rate being very low, the fault dipping angle being unknown and the spatial distribution of GPS sites being non-optimal. Thus here, average left-lateral slip rate of 0.7 ± 0.45 mm/yr and extension rate of 0.6 ± 0.45 mm/yr are obtained by subtracting the average fault-parallel and fault-perpendicular velocities of stations on either side of the fault (Figure 10), resulting in a total relative horizontal displacement rate of 0.9 ± 0.45 mm/yr in the azimuth of 3°.

4. Discussion

4.1. Slip Transfer From the DST to the CFS

[25] The amount and quality of the data used in previous geodetic studies were insufficient for resolving variations in slip rates along the DST north and south of the CFS and identifying changes in ground displacement rates across the CFS. Here, thanks to a large data set, we are able to show that the slip rate along the DST decreases from 4.9 mm/yr (in the range of 4.6–5.9 mm/yr) south of the CFS along the Jericho Valley to 3.8 mm/yr (in the range of 3.1–4.5 mm/yr) north of the CFS. The decrease in slip rate from the Jericho Valley to the northern segment indicates that the Sinai sub-plate is not behaving as a single rigid block, but instead is undergoing internal deformation. In the previous section we showed that stations north of the Carmel Fault are moving to the NNW (azimuth is 3° degrees) at a rate of 0.9 ± 0.45 mm/yr with respect to stations south of that fault. This motion is consistent with the 1.1 mm/yr decrease in slip rate from the Jericho Valley to the northernmost segment. Thus, the present study provides geodetic confirmation of previous suggestions, based on differences in topography, seismic activity and crustal structure, that the CFS divides the Sinai sub-plate into two micro-plates [e.g., *Ben-Avraham and Ginzburg*, 1990; *Hofstetter et al.*, 1991], one north of Carmel-Gilboa line and the other south of the Carmel-Faria line (Figure 5), and that part of the slip between Arabia and Sinai is being transferred from the DST to the CFS.

[26] Interestingly, not only does the present-day slip rate along the DST decreases from the Arava-Jericho segments to the northern segment, but also the geological slip rates seem to be decreasing northward from a total offset of 105 km south of the Dead Sea [*Quennell*, 1959; *Freund et al.*, 1968], to less than 75 km north of the Yammouneh Fault [*Freund et al.*, 1970; *Trifonov et al.*, 1983] (Figure 1). *Freund et al.* [1970] suggested that some of the missing offset is accounted for by the internal deformation of the Sinai sub-plate, including left lateral slip rate along the Carmel Fault and N-S extension across E-W trending normal faults in the Galilee. The current velocity field (Figure 5) clearly indicates that present-day intra-plate horizontal deformation is mostly accommodated by the CFS. Our data, however, cannot resolve whether some N-S extension is also being accommodated by the Galilee's normal fault system [*Ron et al.*, 1984; *Matmon et al.*, 2003].

4.2. Comparison Between Locking and Earthquake Cutoff Depths

[27] Earthquake cutoff depth, i.e. the depth below which the amount of seismic moment release is negligible, is indicative of the seismogenic zone thickness. It is therefore instructive to compare the geodetically determined locking depth and earthquake cutoff depth [*Nazareth and Hauksson*, 2004; *Wdowinski*, 2009; *Smith-Konter et al.*, 2011]. The locking depths obtained in this study are 7.8–16.5 km north of the CFS, 5.9–13.4 km along the Jordan Fault alone, 11.8–24 km along the Jericho Valley, 12–17.6 km along the eastern strand of the Dead Sea, and 12.1–23 km along the Arava Valley. These locking depths and the seismicity cutoff depth of each segment are compared separately. The histograms in Figure 11 show the percentage of seismic moment release as a function of depth for $m_d \geq 2$ that are listed in the Geophysical Institute of Israel (GII) seismic catalog between 1985 and 2010 (note that the GII reported depth error is ±5 km). Similar to other continental transforms, the seismic activity along the DST is limited to the upper crust. A good agreement is found between the geodetically determined locking depth (solid lines) and the depth above which 90% of the seismic moment has been released (dotted lines). The consistency between the two independent data sets suggests that the geodetically determined locking depths are reasonable.

4.3. Implications for Seismic Hazard

4.3.1. The Jordan Fault

[28] Thanks to the large number of near-fault GPS sites distributed on either side of the fault and EDM measurements

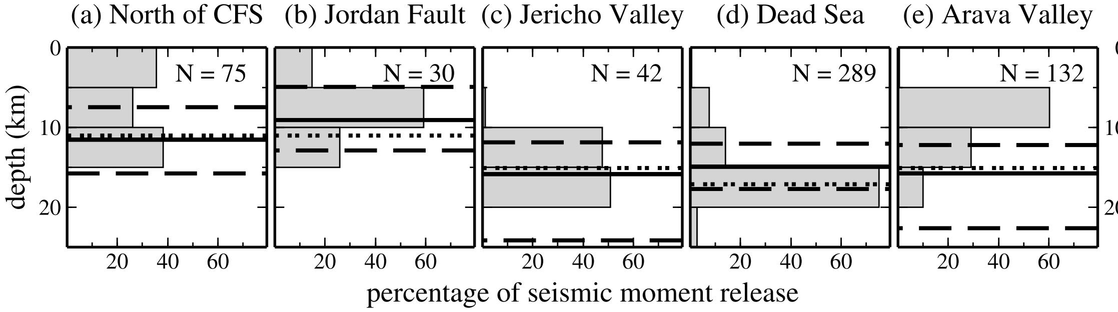

Figure 11. Percentage of seismic moment release as a function of depth along the following segments: (a) north of the CFS, (b) the Jordan Fault, (c) Jericho Valley (d) Dead Sea Basin and (e) Arava Valley. Earthquake data is extracted from the GII catalog, and include $m_d \geq 2$ that occurred between 1985 and 2010. The black solid line denotes the geodetically determined locking depth, with dashed lines indicating the 1σ confidence level. The locking depth shown on Figure 11d is for a scenario where the relative plate motion is accommodated only along the eastern strand of the Dead Sea basin. The dotted lines indicate the depth above which 90% of the seismic moment has been released. The number of earthquakes included in the calculation of the seismic moment, *N*, is shown at the top-right corner of each panel.

[*Even-Tzur and Hamiel*, 2011] in this area we can rule out the possibility of near surface creep, and the picture that emerges for the Jordan Fault is rather clear. During interseismic times this fault is locked down to a depth of 8.7 km (5.9-13.4 km at 68% confidence level). Hence, the slip deficit along this fault is simply equal to the product of the time since the last large earthquake along that segment (an earthquake whose rupture reached the bottom of the seismogenic layer) and the long-term slip rate.

[29] Archeo-seismic studies clearly indicate that two large earthquakes ruptured this segment in historic time. The first is a M > 7 that ruptured in 1202 and displaced an EW trending wall of the crusader Ateret fortress by ~1.6 m and the second is a M~6.6 that ruptured in 1759 and displaced a post-crusader structure by ~0.5 m [*Ellenblum et al.*, 1998]. Thus the minimum slip deficit along the Jordan Fault amounts to 2.5 m since 1202 (810 years times 3.7 mm/yr less 500 mm of subsequent event) or ~0.9 m since 1759. According to *Wells and Coppersmith* [1994] such slip deficits correspond to earthquake magnitudes between 7 and 7.4 ($M = 7.04 + 0.89 \cdot \log(AD)$, where *M* and *AD* are the magnitude and the average displacement, respectively).

4.3.2. The Jericho Valley

[30] Our data clearly indicates that strain is currently being accumulated along this segment. Furthermore, several paleoseismic studies identified the Jericho Fault and found evidence for a few episodic slips [*Reches and Hoexter*, 1981; *Lazar et al.*, 2010], suggesting that several cycles of stick-slip have occurred along this fault in the past. Yet, owing to the sparseness of GPS stations near the Jericho Fault, our data cannot rule out near surface creep. In addition, because the location of the latest historical earthquake in this region is not well known (i.e., the 1546 earthquake [*Ambraseys and Karcz*, 1992; *Ambraseys*, 2009]), the time of the last rupture on the Jericho Fault is uncertain. Consequently, the slip deficit along the Jericho Fault cannot be assessed at the same confidence level as that of the Jordan Fault.

4.3.3. The Dead Sea Basin

[31] Two out of the three strongest instrumentally recorded earthquakes in the entire study area occurred beneath the Dead Sea; the M 6.3 1927 earthquake [*Shapira et al.*, 1993; *Avni et al.*, 2002] and the M 5.1 2004 earthquake [*Hofstetter et al.*, 2008]. It is therefore clear that the potential for moderate-large earthquakes in this area is large. Because earthquakes in this region are not limited to distinct fault locations or dominant focal mechanisms [*Shamir*, 2006; *Hofstetter et al.*, 2007; *Kagan et al.*, 2011] and Holocene faulting was identified on both the eastern and the western strands of the Dead Sea [*Bartov and Sagy*, 2004; *Bartov et al.*, 2006], the manner by which the total slip between Sinai and Arabia is accommodated within the Dead Sea Basin is not fully understood. Furthermore, the absence of displacement gradient from the Mediterranean Sea toward the Dead Sea Western strand implies that this fault is either not slipping left-laterally, or is creeping all the way to the surface. For these reasons the assessment of the slip deficit along the Dead Sea Basin is not straightforward.

4.3.4. The Arava Valley

[32] The good agreement between the observed displacement profiles shown here, in *Le Beon et al.* [2008] and in *Al-Tarazi et al.* [2011], and the locked fault predicted profile strongly suggests that the fault is locked down to 15.5 km (12.1–23 km at 68% confidence level) and is slipping at a rate of 5.1 mm/yr (4.7–5.4 mm/yr at 68% confidence level; Figure 9d). In contrast, surface subsidence at extensional steps detected using InSAR measurements between 1995–2000 suggests that during that time 30–50% of the 5.1 mm/yr were released aseismically [*Finzi*, 2005]. That neither *Le Beon et al.* [2008] nor *Al-Tarazi et al.* [2011] identified such creep, strongly suggests that the deformation reported by [*Finzi*, 2005] is limited in time and space.

[33] Archeo-seismic data indicate that the most recent large earthquake along the northern Arava Valley (Figure 7) was a magnitude 6.5–7 earthquake that occurred in 1458 [*Niemi et al.*, 2001; *Guidoboni and Comastri*, 2005; *Ambraseys*, 2009], and paleoseismic and historic records indicate that the most recent large earthquake along the southern Arava Valley (Avrona fault, Figure 7) was a magnitude 7 earthquake that occurred in 1068 [*Zilberman et al.*, 2005; *Ambraseys*, 2009]. Together with our geodetic slip rate of 5.1 mm/year, the data imply an accumulated slip deficit of ~2.8 m for the northern Arava Valley and ~4.8 m for the Avrona Fault.

These slip deficits correspond to magnitude deficits of 7.4 and 7.6, respectively [*Wells and Coppersmith*, 1994].

4.3.5. The Carmel Fault

[34] Geologic and geomorphic data indicate that the total motion along the Carmel Fault is oblique, implying left-lateral implying horizontal and normal dip-slip components of motion [*de Sitter*, 1962; *Freund et al.*, 1970; *Achmon*, 1986]. Paleoseismic and archeoseismic evidence show that the region nearby the Carmel Fault has experienced severe ground shaking in the past 10 Ka [*Marco et al.*, 2006; *Braun et al.*, 2010]. Although this ground shaking may be caused by a strong earthquake along the DST, the possibility that the damage is related to a moderate to large earthquake along the Carmel Fault cannot be ruled out. In addition, the M 5.3 earthquake that occurred in 1984 between the Carmel Fault and the Izra'el Valley [*Hofstetter et al.*, 1996] (Figure 5) suggests that this region is currently active and may produce moderate earthquakes. While the results of previous geodetic studies were ambiguous [*Agmon*, 2001; *Ostrovsky*, 2005; *Reinking et al.*, 2011] the results obtained in this study clearly indicate a left-lateral sense of slip accompanied by fault-normal extension. Thus, elastic strain is currently being accumulated, and the possibility of moderate-to-large earthquakes along the Carmel Fault cannot be ruled out.

5. Summary and Conclusions

[35] GPS measurements of the 145 survey stations and 18 permanent stations in Israel between 1996 and 2008 shed light on the inter-seismic deformation associated with the DST and the CFS. We find that the slip rate along the DST decreases from ~5 mm/yr along the Jericho Valley, the Dead Sea Basin and the Arava Valley in the south to 3.8 mm/yr along the Kinnarot Valley, Jordan Fault and Hula Basin in the north. By subtracting the average velocity of sites north of the Carmel Fault from that of sites south of the fault we identify an oblique motion along the Carmel Fault with ~0.7 mm/yr left-lateral and ~0.6 mm/yr extension rates. This observation together with the decrease in slip velocity from 4.9 mm/yr along the Jericho Valley to 3.8 mm/yr along the northern segment suggest that north of the CFS, the total slip between Sinai and Arabia is distributed along both the DST and the CFS.

[36] Near-fault site velocities show that there is no shallow creep along the Jordan Fault, and probably not along the Arava Valley as well. There is a possibility that creep occurs along the western strand of the DST in the Dead Sea Basin, but more data regarding the near fault deformation zone, especially within the Dead Sea Basin, is needed for this issue to be resolved.

[37] The results obtained in this study further improve our view of the slip distribution along the major faults in the southern Levant, especially along the DST northern segment, where these parameters are extremely well constrained. Additional near fault measurements from either side of the DST are necessary in order to assess the extent to which strain is released by either continuous or episodic aseismic slip along the Jericho Valley and the Dead Sea Basin.

[38] **Acknowledgments.** We thank G. Bear, I. Haviv, Z. Garfunkel, Y. Eyal, S. Marco, R. Nof, A. Inbal and S. Shani-Kadmiel for fruitful discussion and their comments on an early version of this paper; R. W. King and the SOPAC group for assisting with the data processing; M. Rozenblum, G. Even-Tzur and L. Shahar for providing the data; Y. Mizrachi, and R. Knafo for assisting with the field work. Y. Hamiel acknowledges support by the US-Israel Binational Science Foundation (BSF) grant number 2008248. Finally, we thank the Associate Editor I. Ryder and two anonymous reviewers for their constructive remarks.

References

Achmon, M. (1986), The Carmel boundary fault between Yokneam and Nesher (in Hebrew), MSc thesis, Hebrew Univ., Jerusalem.

Agmon, A. (2001), Algorithm for the analysis of deformation monitoring networks (in Hebrew), MSc thesis, Technion, Haifa, Israel.

Aldersons, F., Z. Ben-Avraham, A. Hofstetter, E. Kissling, and T. Al-Yazjeen, (2003), Lower-crustal strength under the Dead Sea basin from local earthquake data and rheological modeling, *Earth Planet. Sci. Lett.*, *214*, 129–142, doi:10.1016/S0012-821X(03)00381-9.

Al-Tarazi, E., J. Abu-Rajab, F. Gomez, W. Cochran, R. Jaafar, and M. Ferry (2011), GPS measurements of near-field deformation along the southern Dead Sea Fault System, *Geochem. Geophys. Geosyst.*, *12*, Q12021, doi:10.1029/2011GC003736.

Ambraseys, N. N. (2009), *Earthquakes in the Mediterranean and Middle East: A Multidisciplinary Study of Seismicity up to 1900*, Cambridge Univ. Press, Cambridge, U. K.

Ambraseys, N. N., and I. Karcz (1992), The earthquake of 1546 in the Holy Land, *Terra Nova*, *4*(2), 254–263, doi:10.1111/j.1365-3121.1992.tb00480.x.

Avni, R., D. Bowman, A. Shapira, and A. Nur (2002), Erroneous interpretation of historical documents related to the epicenter of the 1927 Jericho earthquake in the Holy Land, *J. Seismol.*, *6*, 469–476, doi:10.1023/A:1021191824396.

Bartov, Y., and A. Sagy (2004), Late Pleistocene extension and strike-slip in the Dead Sea Basin, *Geol. Mag.*, *141*(5), 565–572, doi:10.1017/S001675680400963X.

Bartov, Y., A. Sneh, L. Fleischer, and M. Rosensaft (2000), Map of potentially active faults, *Rep. GSI/23/2000*, Geol. Surv. of Isr., Jerusalem.

Bartov, Y., et al. (2006), Late Quaternary faulting and subsidence in the central Dead Sea Basin, *Isr. J. Earth Sci.*, *55*, 17–31.

Ben-Avraham, Z., and A. Ginzburg (1990), Displaced terranes and crustal evolution of the Levant and the eastern Mediterranean, *Tectonics*, *9*(4), 613–622, doi:10.1029/TC009i004p00613.

Braun, Y., E. Kagan, M. Bar-Matthews, A. Ayalon, and A. Agnon (2010), Dating speleoseismites near the Dead Sea Transform and the Carmel fault: Clues to coupling of a plate boundary and its branch, *Isr. J. Earth Sci.*, *58*, 257–273, doi:10.1560/IJES.58.3-4.257.

de Sitter, L. U. (1962), Structural development of the Arabian sheild in Palestine, *Geol. Mijnb.*, *45*, 116–124.

Ellenblum, R., S. Marco, A. Agnon, T. Rockwell, and X. Boas (1998), Crusader castle torn apart by earthquake at dawn, 20 May 1202, *Geology*, *26*, 303–306.

Even-Tzur, G., and Y. Hamiel (2011), Geodetic study of crustal deformation across the Dead Sea Fault system in the Jordan Gorge area, Northern Israel, *Isr. J. Earth Sci.*, *58*, 193–201.

Eyal, M., Y. Eyal, Y. Bartov, and G. Steinitz (1981), The tectonic development of the western margin of the Gulf of Elat (Aqaba) rift, *Tectonophysics*, *80*, 39–66, doi:10.1016/0040-1951(81)90141-4.

Finzi, Y. (2005), Current deformation in the southern Dead Sea Transform: Radar interferometry measurements and their tectonic implications, *Rep. GSI/24/04*, Geol. Surv. of Isr., Jerusalem.

Freund, R., I. Zak, and Z. Garfunkel (1968), Age and rate of the sinistral movement along the Dead Sea rift, *Nature*, *220*, 253–255.

Freund, R., Z. Garfunkel, I. Zak, M. Goldberg, T. Weisbrod, and B. Derin (1970), The shear along the Dead Sea rift, *Philos. Trans. R. Soc. London, Ser. A*, *267*, 107–130.

Garfunkel, Z. (1981), Internal structure of the Dead Sea leaky transform (rift) in relation to plate kinematics, *Tectonophysics*, *80*, 81–108, doi:10.1016/0040-1951(81)90143-8.

Garfunkel, Z., and Z. Ben-Avraham (1996), The structure of the Dead Sea basin, *Tectonophysics*, *266*, 155–176, doi:10.1016/S0040-1951(96)00188-6.

Garfunkel, Z., I. Zak, and R. Freund (1981), Active faulting in the Dead Sea rift, *Tectonophysics*, *80*, 1–26, doi:10.1016/0040-1951(81)90139-6.

Guidoboni, E., and A. Comastri (2005), *Catalogue of Earthquakes and Tsunamis in the Mediterranean Area From the 11th to the 15th Century*, Ist. Naz. di Geofis. e Vulcanol., Bologna, Italy.

Herring, T. A., R. W. King, and S. C. McClusky (2009), Documentation of the GAMIT and GLOBK GPS analysis software release 10.3, report, 206 pp., Mass. Inst. of Technol., Cambridge.

Hofstetter, A., L. Feldman, and Y. Rotstein (1991), Crustal structure of Israel: Constraints from teleseismic and gravity data, *Geophys. J. Int.*, *104*, 371–379, doi:10.1111/j.1365-246X.1991.tb02517.x.

Hofstetter, A., T. van Eck, and A. Shapira (1996), Seismic activity along fault branches of the Dead Sea-Jordan Transform System: The Carmel-Tirtza fault system, *Tectonophysics*, *267*, 317–330, doi:10.1016/S0040-1951(96)00108-4.

Hofstetter, R., Y. Klinger, A. Q. Amrat, L. Rivera, and L. Dorbath (2007), Stress tensor and focal mechanisms along the Dead Sea fault and related structural elements based on seismological data, *Tectonophysics*, *429*, 165–181, doi:10.1016/j.tecto.2006.03.010.

Hofstetter, R., Y. Gitterman, V. Pinksy, N. Kraeva, and L. Feldman (2008), Seismological observations of the northern Dead Sea basin earthquake on 11 February 2004 and its associated activity, *Isr. J. Earth Sci.*, *57*, 101–124, doi:10.1560/IJES.57.2.101.

Hurwitz, S., Z. Garfunkel, Y. Ben-Gai, M. Reznikov, Y. Rotstein, and H. Gvirtzman (2002), The tectonic framework of a complex pull-apart basin: Seismic reflection observations in the Sea of Galilee, Dead Sea transform, *Tectonophysics*, *359*, 289–306, doi:10.1016/S0040-1951(02)00516-4.

Joffe, S., and Z. Garfunkel (1987), Plate kinematics of the circum Red Sea—A re-evaluation, *Tectonophysics*, *141*, 5–22, doi:10.1016/0040-1951(87)90171-5.

Kagan, E., M. Stein, A. Agnon, and F. Neumann (2011), Intrabasin paleoearthquake and quiescence correlation of the late Holocene Dead Sea, *J. Geophys. Res.*, *116*, B04311, doi:10.1029/2010JB007452.

Klinger, Y., J. P. Avouac, N. Abouh Karaki, and N. Tisnerat (2000), Seismic behaviour of the Dead Sea fault along Araba valley, Jordan, *Geophys. J. Int.*, *142*, 769–782, doi:10.1046/j.1365-246x.2000.00166.x.

Lazar, M., Z. Ben-Avraham, and U. Schattner (2006), Formation of sequential basins along a strike slip fault—Geophysical observations from the Dead Sea basin, *Tectonophysics*, *741*, 53–69, doi:10.1016/j.tecto.2006.04.007.

Lazar, M., Z. Ben-Avraham, Z. Garfunkel, N. Porat, and S. Marco (2010), Is the Jericho Escarpment a tectonic or a geomorphological feature? Active faulting and paleoseismic trenching, *J. Geol.*, *118*(3), 261–276, doi:10.1086/651504.

Le Beon, M., Y. Klinger, A. Q. Amrat, A. Agnon, L. Dorbath, G. Baer, J.-C. Ruegg, O. Charade, and O. Mayyas (2008), Slip rate and locking depth from GPS profiles across the southern Dead Sea Transform, *J. Geophys. Res.*, *113*, B11403, doi:10.1029/2007JB005280.

Makovsky, Y., A. Wunch, R. Ariely, Y. Shaked, A. Rivlin, A. Shemesh, Z. Ben-Avraham, and A. Agnon (2008), Quaternary transform kinematics constrained by sequence stratigraphy and submerged coastline features: The Gulf of Aqaba, *Earth Planet. Sci. Lett.*, *271*, 109–122, doi:10.1016/j.epsl.2008.03.057.

Mao, A., C. G. A. Harrison, and T. H. Dixon (1999), Noise in GPS coordinate time series, *J. Geophys. Res.*, *104*, 2797–2816, doi:10.1029/1998JB900033.

Marco, S., A. Agnon, R. Ellenblum, A. Eidelman, U. Basson, and A. Boas (1997), 817-year-old walls offset sinistrally 2.1 m by the Dead Sea transform, Israel, *J. Geodyn.*, *24*, 11–20, doi:10.1016/S0264-3707(96)00041-5.

Marco, S., T. Rockwell, A. Heimann, U. Frieslander, and A. Agnon (2005), Late Holocene activity of the Dead Sea Transform revealed in 3D palaeoseismic trenches on the Jordan Gorge segment, *Earth Planet. Sci. Lett.*, *234*, 189–205, doi:10.1016/j.epsl.2005.01.017.

Marco, S., A. Agnon, I. Finkelstein, and D. Ussishkin (2006), Megiddo earthquakes, in *Megiddo IV: The 1998–2002 Seasons*, *Emery and Claire Yass Publ. Archaeol. Ser.*, vol. 24, chap. 31, pp. 569–575, Inst. of Archaeol., Tel Aviv Univ., Tel Aviv, Israel.

Matmon, A., S. Wdowinski, and J. K. Hall (2003), Morphological and structural relations in the Galilee extensional domain, northern Israel, *Tectonophysics*, *371*, 223–241, doi:10.1016/S0040-1951(03)00237-3.

McClusky, S., R. Reilinger, S. Mahmoud, D. Ben Sari, and A. Tealeb (2003), GPS constraints on Africa (Nubia) and Arabia plate motions, *Geophys. J. Int.*, *155*, 126–138, doi:10.1046/j.1365-246X.2003.02023.x.

Melzer, Y. (1996), The establishment of geodetic–geodynamic network in Israel (in Hebrew), paper presented at Geodesy and Surveying Symposium, Technion, Haifa, Israel.

Nazareth, J. J., and E. Hauksson (2004), The seismogenic thickness of the Southern California crust, *Bull. Seismol. Soc. Am.*, *94*, 940–960, doi:10.1785/0120020129.

Niemi, T. M., H. Zhang, M. Atallah, and J. B. J. Harrison (2001), Late Pleistocene and Holocene slip rate of the Northern Wadi Araba fault, Dead Sea Transform, Jordan, *J. Seismol.*, *5*(3), 449–474, doi:10.1023/A:1011487912054.

Nof, R. (2006), Recent crustal movements along the Carmel Fault System using Interferomeric Synthethic Aperture Radar (InSAR) (in Hebrew with English abstract), MSc thesis, Ben-Gurion Univ., Be'er Sheva, Israel.

Ostrovsky, E. (2005), The G1 geodetic-geodynamic network: Results of the G1 GPS surveying campaigns in 1996/1997 and 2001/2002, report, 50 pp., Sur. of Isr., Tel Aviv, Israel.

Picard, L., and E. Kashai (1958), On the lithostratigraphy and tectonics of the Carmel, *Bull. Res. Counc. Israel*, *7G*, 1–19.

Quennell, A. M. (1959), Tectonics of the Dead Sea rift, paper presented at 20th International Geological Congress, Assoc. Serv. Geol. Afr., Mexico City.

Reches, Z., and D. F. Hoexter (1981), Holocene seismic and tectonic activity in the Dead Sea area, *Tectonophysics*, *80*, 235–254, doi:10.1016/0040-1951(81)90151-7.

Reilinger, R., et al. (2006), GPS constraints on continental deformation in the Africa-Arabia-Eurasia continental collision zone and implications for the dynamics of plate interactions, *J. Geophys. Res.*, *111*, B05411, doi:10.1029/2005JB004051.

Reinking, J., S. P. Hillrich, G. Even-Tzur (2011), Surface deformation along the Carmel Fault System, Israel, *J. Geodyn.*, *52*, 321–331, doi:10.1016/j.jog.2011.03.004.

Ron, H., R. Freund, and Z. Garfunkel (1984), Block rotation by strike-slip faulting: Structural and paleomagnetic evidence, *J. Geophys. Res.*, *89*, 6256–6270.

Rotstein, Y., and Y. Bartov (1989), Seismic reflection across a continental transform: An example from a convergent segment of the Dead Sea rift, *J. Geophys. Res.*, *94*, 2902–2912, doi:10.1029/JB094iB03p02902.

Savage, J. C., and R. O. Burford (1973), Geodetic determination of relative plate motion in central California, *J. Geophys. Res.*, *78*, 832–845, doi:10.1029/JB078i005p00832.

Shamir, G. (2006), The active structure of the Dead Sea Depression, *Spec. Pap. Geol. Soc. Am.*, *401*, 15–32, doi:10.1130/2006.2401(02).

Shapira, A., R. Avni, and A. Nur (1993), A new estimate for the epicenter of the Jericho earthquake of 11 July 1927, *Isr. J. Earth Sci.*, *42*, 93–96.

Smith-Konter, B., D. Sandwell, and P. Shearer (2011), Comparison of locking depths estimated from geodesy and seismology along the San Andreas Fault System, *J. Geophys. Res.*, *116*, B06401, doi:10.1029/2010JB008117.

Trifonov, V., A. Youssef, Y. Al-Khair, and T. Zaza (1983), Using satellite imagery to infer the tectonics and the petroleum geology of Syria, report, 18 pp., Syr. Pet. Co., Damascus.

van Eck, T., and A. Hofstetter (1990), Fault geometry and spatial clustering of microearthquakes along the Dead Sea-Jordan rift fault zone, *Tecotonophysics*, *180*, 15–27, doi:10.1016/0040-1951(90)90368-I.

Vigny, C., P. Huchon, J. C. Ruegg, K. Khanbari, and L. M. Asfaw (2006), Confirmation of Arabia plate slow motion by new GPS data in Yemen, *J. Geophys. Res.*, *111*, B02402, doi:10.1029/2004JB003229.

Wdowinski, S. (2009), Deep creep as a cause for the excess seismicity along the San Jacinto fault, *Nat. Geosci.*, *2*, 882–885, doi:10.1038/ngeo684.

Wdowinski, S., Y. Bock, Y. Forrai, Y. Melzer, and G. Baer (2001), The GIL network of continuous GPS monitoring in Israel for geodetic and geophysical applications, *Isr. J. Earth Sci.*, *50*, 39–47.

Wdowinski, S., Y. Bock, G. Baer, L. Prawirodirdjo, N. Bechor, S. Naaman, R. Knafo, Y. Forrai, and Y. Melzer (2004), GPS measurements of current crustal movements along the Dead Sea Fault, *J. Geophys. Res.*, *109*, B05403, doi:10.1029/2003JB002640.

Wells, D. L., and K. J. Coppersmith (1994), New empirical relationships among magnitude, rupture length, rupture width, rupture area and surface displacement, *Bull. Seismol. Soc. Am.*, *84*, 974–1002.

Zhang, J., Y. Bock, H. Jhonson, P. Fang, S. Williams, J. Genrich, S. Wdowinski, and J. Behr (1997), Southern California permanent GPS geodetic array: Error analysis of daily position estimates and site velocities, *J. Geophys. Res.*, *102*(B8), 18,035–18,055, doi:10.1029/97JB01380.

Zilberman, E., R. Amit, N. Porat, Y. Enzel, and U. Avner (2005), Surface ruptures induced by the devastating 1068 AD earthquake in the Southern Arava Valley, Dead Sea Rift, Israel, *Tectonophysics*, *408*, 79–99, doi:10.1016/j.tecto.2005.05.030.